AGU PUBLICATIONS

JGR

Journal of Geophysical Research: Space Physics

RESEARCH ARTICLE

10.1002/2014JA019788

Key Points:

- Observations of the nightside Martian ionosphere by the fix spacing MARSIS radar sounder
- The ionospheric peak densities increase for larger upstream dynamic pressures
- Very high peak densities are often associated with westward IMF

Correspondence to:
C. Diéval,
catherine-dieval@uiowa.edu

Citation:
Diéval, C., D. D. Morgan, F. Němec, and D. A. Gurnett (2014), MARSIS observations of the Martian nightside ionosphere dependence on solar wind conditions, *J. Geophys. Res. Space Physics*, *119*, 4077–4093, doi:10.1002/2014JA019788.

Received 15 JAN 2014
Accepted 29 APR 2014
Accepted article online 7 MAY 2014
Published online 27 MAY 2014

MARSIS observations of the Martian nightside ionosphere dependence on solar wind conditions

C. Diéval[1], D. D. Morgan[1], F. Němec[2], and D. A. Gurnett[1]

[1]Department of Physics and Astronomy, University of Iowa, Iowa City, Iowa, USA, [2]Faculty of Mathematics and Physics, Charles University in Prague, Prague, Czech Republic

Abstract Despite the absence of solar radiation on the Martian nightside, a weak, irregular, and variable ionosphere is produced there. The nightside ionosphere is thought to be maintained by two main sources: dayside-nightside plasma transport and electron precipitation. Observations by Mars Express (MEX) and Mars Global Surveyor (MGS) have shown that these plasma sources are either hindered or favored by the presence of strong crustal magnetic fields and that these effects are modulated by external parameters, such as the solar wind dynamic pressure and the orientation of the interplanetary magnetic field (IMF). These external drivers are expected to influence the supply of plasma to the nightside and thus the formation of the irregular nightside ionosphere. We here present a statistical study of the Martian ionosphere at solar zenith angle greater than 107° from November 2005 to May 2006, using remote measurements of ionospheric echoes with the Mars Advanced Radar for Subsurface and Ionospheric Sounding (MARSIS) radar sounder onboard MEX and using MGS-based proxies for the solar wind dynamic pressure and the IMF clock angle. We find that the peak densities increase with the dynamic pressure and also that cases of very high peak density are almost always associated with Westward IMF orientation. We find that, using MEX/ASPERA-3 electron data, these cases often seem to be linked to accelerated electrons. Plasma transport is known to be important in the near nightside. On the other hand, electron precipitation prevails when the dynamic pressure is high enough to compress the ionosphere and in vertical field regions where the IMF orientation matters.

1. Introduction

In the absence of a global planetary magnetic field, the conductive Martian ionosphere diverts the upstream solar wind flow, which causes a bow shock to form and the flow to slow down and heat up in the region called the magnetosheath. When the interplanetary magnetic field (IMF), carried by the solar wind, penetrates the topside ionosphere, it induces currents and magnetic fields and begins to drape and pile up on the dayside. A region of strong magnetic field forms, called the magnetic barrier or magnetic pileup region, where the magnetic field is mostly horizontal on the dayside but becomes more radial on the nightside. The draped IMF is carried over the "magnetic poles" by the solar wind and stretches tailward on the nightside due to atmospheric mass loading of the flow. Magnetic tension forces push the field lines behind the planet to form the magnetotail with two lobes of opposite polarity, controlled by the IMF orientation. The plasma sheet separates the lobes. For more details see, e.g., the review by *Nagy et al*. [2004, and references therein].

Data from the Magnetometer-Electron Reflectometer (MAG-ER) onboard Mars Global Surveyor (MGS) have established the existence of remanent dipole-like crustal magnetic fields [e.g., *Acuña et al*., 1999]. Weak fields exist in the North ($B < 50$ nT at 400 km) while the South is dominated by strong crustal fields localized at 150–210° East longitude ($B > 50$ nT at 400 km).

Zhang et al. [1990] report that a significant ionospheric peak was detected on the nightside only 40% of the time through radio occultation measurements by Viking, being too low to be detected otherwise. The measured peak electron densities were of the order of 5000 cm^{-3}, ~30 times smaller than values reported in the subsolar region by *Morgan et al*. [2008]. In the absence of photoionization, other sources are considered to supply the nightside ionosphere, mainly electron precipitation and ionospheric plasma transport from dayside to nightside [*Fox et al*., 1993].

Using radio occultation measurements by the Mars Express Radio Science Experiment, *Withers et al*. [2012] find that the trends of the peak densities and peak altitudes as a function of solar zenith angle (SZA) agree

©2014. American Geophysical Union. All Rights Reserved.

with plasma transport being important up to SZA of 115°. *Němec et al*. [2010] have used data from the Mars Advanced Radar for Subsurface and Ionospheric Sounding (MARSIS) onboard Mars Express (MEX) and determined that the peak densities decrease when SZA increases from 107 to 125° in regions of low crustal field, while there is no SZA dependence in regions of strong crustal field. They suggest that the plasma transport to the nightside is hindered by large vertical crustal fields.

Withers et al. [2012] also mention that the peak altitudes ≥150 km measured at SZA > 115° are consistent with peak altitudes from impact ionization by electron precipitation as predicted by models [e.g., *Fillingim et al*., 2007]. Calculations of ionization rates due to electron precipitation were carried out by, e.g., *Fillingim et al*. [2007], who find that an accelerated/peaked electron spectrum (with fluxes peaking at ~100 eV or more) causes a larger peak density 3 times larger than a magnetotail spectrum (a heated spectrum with energies from ~10 eV to ~100 eV). *Lillis et al*. [2009] also find that crustal magnetic field configurations have significant effects on modeled electron peak densities and ionization rates. Indeed, MARSIS measurements indicate elevated values of the ionospheric total electron content (TEC) above vertical crustal magnetic fields for SZA of 100–130° [*Safaeinili et al*., 2007]. In addition, MARSIS observes the nightside ionosphere 4 times more often for vertical crustal magnetic fields than for horizontal fields [*Němec et al*., 2010]. Finally, electron peak densities reach values of the order of 10^4 cm^{-3} above strong magnetic anomalies [*Němec et al*., 2010]. The common interpretation is that in vertical magnetic field regions, open magnetic field lines form that connect the crustal fields to the solar wind. These open field lines allow precipitating auroral or magnetotail electrons to reach low altitudes and to cause localized heating and ionization of the atmosphere.

Observations by MEX and MGS have shown that the penetration of suprathermal electrons (energy from ~10 to ~100 s of eV) to low altitudes depends strongly on the crustal field strength and orientation. For example, the boundary separating the planetary plasma from the solar wind plasma, the induced magnetosphere boundary, is measured at higher altitudes above large magnetic anomalies than above low-field regions [e.g., *Brain et al*., 2005; *Crider et al*., 2002]. The minimum altitude reached by solar wind electrons increases as the crustal field strength increases [e.g., *Fränz et al*., 2006]. The reason is that the large magnetic pressure due to these magnetic anomalies contributes to raising the altitude at which the solar wind pressure balances the ionospheric pressure. On the Martian nightside, spikes of suprathermal electrons (short duration < ~1 min) are observed above magnetic cusps [e.g., *Dubinin et al*., 2008a; *Mitchell et al*., 2001], which suggests that vertical fields facilitate the access of precipitating electrons to the atmosphere. Such access can occur when the orientations of the IMF and crustal fields are favorable to magnetic reconnection. Indeed, observations of solar wind electron spikes above the strong field regions are more frequent when the IMF points dawnward [e.g., *Dubinin et al*., 2008b]. In addition, peaked electron distributions of auroral type are observed at the boundary between open and closed field lines, preferably when the IMF points dawnward, which suggests magnetic reconnection [e.g., *Brain et al*., 2006a]. On the other hand, the regions of horizontal magnetic fields display plasma voids, i.e., very low electron fluxes, meaning that the solar wind has no access to these regions, which allows the plasma to recombine, as the magnetic anomaly rotates from the dayside to the nightside [e.g., *Mitchell et al*., 2001].

Lillis and Brain [2013] have investigated the precipitation patterns of electrons measured by MGS as a function of IMF direction and solar wind dynamic pressure. They find that higher dynamic pressure is associated with higher electron fluxes. The flux increase is more pronounced in the North than in the South, where the atmosphere is locally shielded by significant magnetic anomalies. The electron fluxes do not vary with IMF direction in the weak field regions, because the magnetic field configuration is usually open. Lower electron fluxes are observed above the strong crustal fields for dawnward IMF than for duskward IMF, suggesting that a larger proportion of open field lines is formed when the IMF has a particular orientation, which is more likely when the crustal field is strong [*Lillis and Brain*, 2013].

It is expected that the ionization sources and thus the formation of the nightside ionosphere, vary with changes in the solar wind conditions. In this work, we perform a statistical study of the effects of the IMF clock angle and the solar wind dynamic pressure on the electron peak densities and the occurrence frequency of ionospheric reflections recorded by MARSIS on the nightside. From our results, we will attempt to compare the importance of electron impact ionization versus transterminator plasma flow for supplying plasma to the nightside ionosphere.

Section 2 describes the MARSIS instrument and data and the selection of IMF clock angle and dynamic pressure values. Section 3 reports the results. Section 4 includes the discussion and conclusion.

©2014. American Geophysical Union. All Rights Reserved.

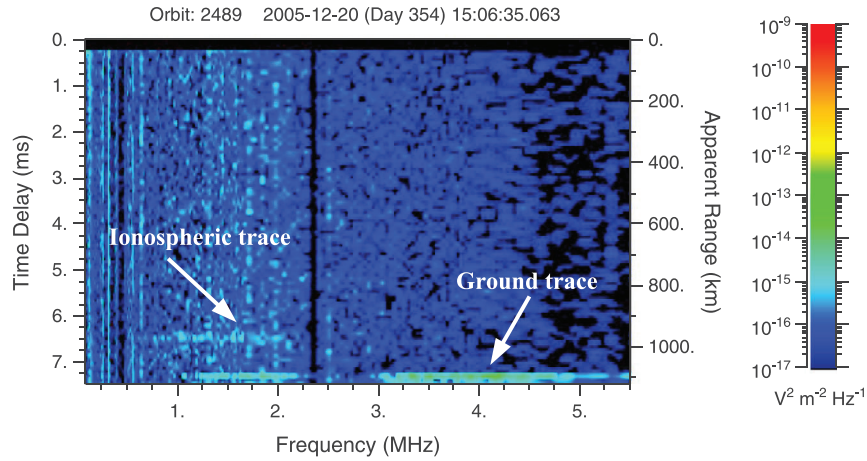

Figure 1. Example of an ionogram, taken on 20 December 2005 at 15:06:35 during orbit 2489. The color unit is the received intensity. The horizontal axis is the sounding frequency. The left vertical axis is the delay time for the reception of the echo, and the right vertical axis is the corresponding apparent range of the echo to the spacecraft. The horizontal line at a fixed range of 1083 km is the echo from the surface of Mars. The horizontal line at a fixed range of 968 km is the echo from the ionosphere.

2. Instrument, Data, and Method

The MARSIS radar sounder operates in two modes (see details in *Picardi et al*. [2004]). The subsurface mode probes the Martian subsurface and the ionospheric mode probes the topside ionosphere. We use the data from the ionospheric mode. MARSIS consists of a 40 m long electric dipole antenna, a transmitter, a receiver, and a digital data processing system. The transmitter sweeps through 160 quasi-logarithmically spaced frequency steps ($\Delta f/f \approx 2\%$) from 0.1 to 5.4 MHz, during 1.26 s. At each step, a 91.4 μs quasi-sinusoidal pulse is transmitted at a fixed frequency f and the intensities of the resulting signal echoes (reflections) are measured as a function of delay time Δt, in 80 equally spaced time bins, from 259.3 μs to 7.86 ms after the start of the sounding pulse. The basic frequency sweep cycle is repeated every 7.54 s. The result is a matrix of 80×160 received intensities, which can be plotted as a frequency-delay time spectrogram, called an ionogram.

Figure 1 shows an example of an ionogram. The reflection from the ionosphere is visible at an apparent range of 968 km. The delay time can be converted to apparent range, defined as the sounding pulse round trip distance assuming no dispersion, by the expression $c \cdot t_{delay}/2$. The corresponding apparent altitude can be calculated as the spacecraft altitude minus the range, i.e., 115 km. Such a value is too low to be real and suggests that the reflection is oblique to the nadir direction [*Němec et al*., 2010]. In addition, the ionospheric trace overlaps the ground trace, which is not possible for a horizontally stratified ionosphere. This means that the echo is not coming from the vertical direction. The existence of such oblique echoes implies that the nightside ionosphere is not laminar but is structured with holes and patches of plasma [*Gurnett et al*., 2008; *Němec et al*., 2010]. The ionospheric trace in Figure 1 extends from 0.76 to 1.7 MHz and has no dependence on the sounding frequency, meaning that the topside ionosphere appears like a "slab" at a given altitude. This slab-like appearance is typical of the observations of the nightside ionosphere by MARSIS [*Němec et al*., 2010]. The highest frequency for which the ionospheric trace is detected is the ionospheric peak frequency f_{max}. Electron peak densities Ne_{max} are retrieved by Ne_{max} [cm^{-3}] $\approx (f_{max}$ [Hz]/8980)^2. In the example here the peak density is $3.6 \cdot 10^4$ cm^{-3}, which is much higher than the values on nightside of the order of 5000 cm^{-3} reported by *Zhang et al*. [1990]. This ionospheric trace was detected in the region of the strongest crustal fields, in the southern hemisphere. *Němec et al*. [2010] report that the largest nightside peak densities are recorded in regions of crustal field strength > 100 nT, possibly due to greater concentration of field lines in these areas which allow more open field lines to form and to carry more precipitating electrons down to the atmosphere.

MARSIS records data at altitudes below 1200 km. The ionospheric echoes can only be detected at altitudes ≤ 1100 km, corresponding to the maximum time delay measured by the radar. We selected data when the spacecraft is at altitudes ≤ 1100 km and SZA > 107°. The first criterion ensures that ionospheric reflections can be detected if they do exist and the second ensures that the ionosphere at 150 km altitude is in darkness. In this work, we also use two solar wind proxies developed from MGS/MAG-ER measurements: an

©2014. American Geophysical Union. All Rights Reserved.

IMF clock angle proxy [*Brain et al*., 2006b] and a solar wind dynamic pressure proxy [*Brain et al*., 2005]. We choose to use MGS data because MEX carries no magnetometer. The time of our analysis is from November 2005 to May 2006, which is the time when MARSIS and MGS measurements overlap, with the required conditions above. Both proxies have 2 h time resolution (period of MGS orbit).

The IMF clock angle proxy [*Brain et al*., 2006b] is the median azimuth angle between the locally horizontal component of the draped magnetic field direction and the local East direction at MGS, counted anticlockwise (90° angle is local North). This azimuth angle uses data from the dayside, in the latitude band where crustal fields are weak (50–60°), and therefore, the main contributor to the magnetic field at that location is the draped external field [e.g., *Brain et al*., 2003]. This proxy is not perfect, but it is a reasonably accurate estimation of the upstream IMF clock angle, to determine in which IMF sector Mars is at a given time [*Brain et al*., 2006b]. The IMF sectors are oriented either dawnward-westward or duskward-eastward, relative to Mars, viewed from the Sun. When the upstream IMF is westward, the draped IMF observed at the MGS location tends to cluster toward the southwest direction, mostly near the 250–270° clock angle [*Brain et al*., 2006b]. However, we are interested in the eastward or westward component of the draped IMF vector, which is assumed to be a reliable proxy of the upstream IMF sector (eastward or westward). We then define the eastward IMF group as clock angle $< 90°$ or clock angle $> 270°$, and the westward IMF group as $90° <$ clock angle $< 270°$.

The dynamic pressure proxy [*Brain et al*., 2005] is obtained by using measurements of the draped magnetic field strength at SZA $< 110°$ and outside regions of strong crustal fields; these measurements are fitted by a cos(SZA) function, and the value at SZA = 0° gives the subsolar magnetic field strength. The proxy is based on the assumption that the magnetic pressure in the magnetic pileup region is the dominant pressure term which can balance the upstream dynamic pressure [*Crider et al*., 2003]. The magnetic field strength increases in the magnetic pileup region as the solar wind dynamic pressure increases. We separate the dynamic pressure proxy into three groups: low pressure during quiet conditions ($B < 30$ nT), moderate pressure during average conditions ($30 \leq B \leq 50$ nT), and high pressure during extreme conditions, prevailing during solar wind pressure pulse impacts on Mars ($B > 50$ nT). In the article, we use the term subsolar magnetic strength B in place of the dynamic pressure proxy.

For each MARSIS ionogram corresponding to the criterion of altitudes ≤ 1100 km and SZA $> 107°$, we select the proxy values measured within 2 h before and after the time of the ionogram. Where such values exist, we take the median as our value of the subsolar magnetic field proxy for this ionogram. Similarly, where such values of the draped IMF azimuth angle proxy exist, we take the first value as the value for this ionogram. There are 8535 ionograms in the data coverage for which the proxy values could be assigned. Among these ionograms, there are 985 ionograms showing an ionospheric echo; this means an occurrence frequency of 11% for the ionospheric echo detection. The electron peak density is often not high enough to be detected by MARSIS, due to the limitations of measurements at low sounding frequencies [*Němec et al*., 2010].

In the next section, we look at the dependence of the nightside ionosphere on the subsolar magnetic field B and IMF clock angle in sections 3.1 and 3.2. In section 3.3, we look in more detail at cases of very high peak electron densities. We note that for the period of study, the SZA range covered by the spacecraft goes up to 130°, with a median of 116°. MEX does not sample the far nightside during the interval of time studied, so we did not attempt to investigate a SZA dependence of the influence of the MGS proxies on the nightside ionosphere.

3. Results

3.1. Dependence on Subsolar Magnetic Strength

Figure 2 investigates the dependence of ionospheric echoes on subsolar B. Figure 2a shows a histogram of the subsolar B values assigned to all the ionograms of the data coverage. There are 2946 ionograms in the low subsolar B group, 4408 ionograms in the moderate subsolar B, and 1181 ionograms in the high subsolar B. The distribution has a median value of 35 nT (within the range of moderate subsolar B defined above) and an extended tail toward high subsolar B values: 14% of the values are > 50 nT up to 101 nT.

Figure 2b compares the distributions of the subsolar B values corresponding to the data coverage (black) and to the ionograms with ionospheric echoes, i.e., with peak densities large enough to be detected by MARSIS (red), with each distribution normalized by its number of ionograms. The distribution for the ionospheric echoes has a median value of ~42 nT and presents an extended tail toward the high subsolar B range (up to 101 nT). There are 228 ionospheric echoes for the low subsolar B range, 534 for moderate subsolar B and 223 for high

©2014. American Geophysical Union. All Rights Reserved.

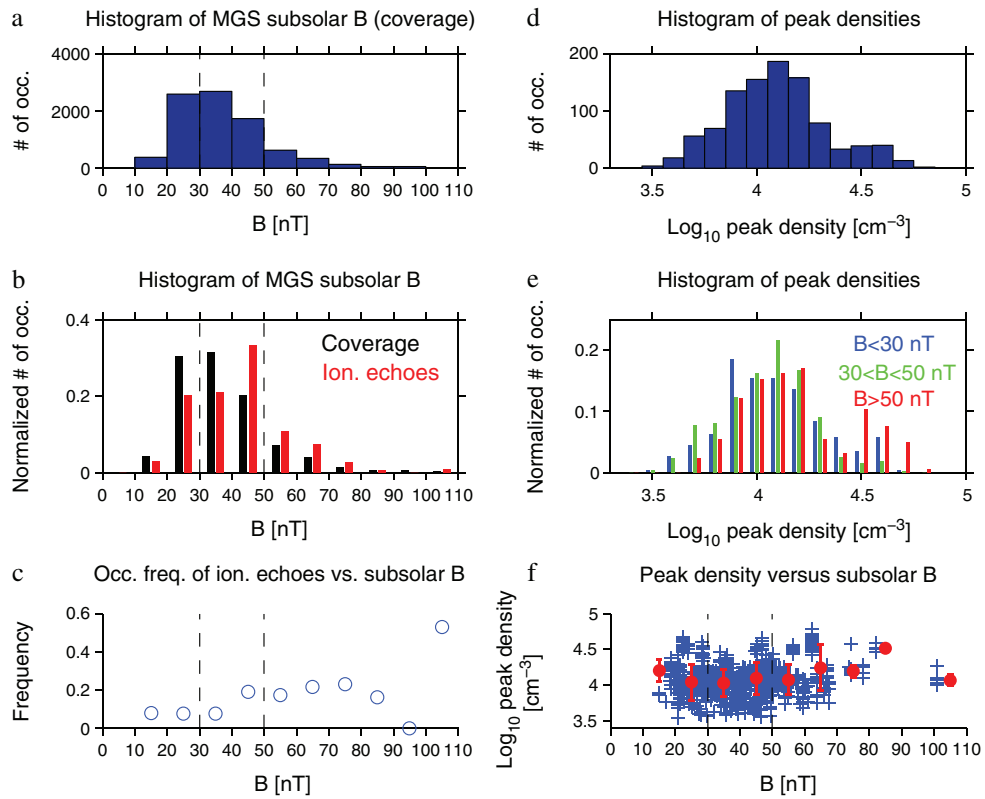

Figure 2. (a) Histogram of subsolar magnetic strength *B* values assigned to the ionograms of the data coverage. The bin size is 10 nT. (b) Histograms of subsolar *B* values assigned to the ionograms of the data coverage (black) and to the ionograms with ionospheric echoes (red). Each distribution is normalized by its number of ionograms. (c) Occurrence frequency of detecting ionospheric echoes binned by the subsolar *B*. (d) Histogram of electron peak densities for the ionospheric echoes. The bin size is 0.1 in logarithmic scale. (e) Histograms of electron peak densities for the ionospheric echoes, sorted in 3 groups: low subsolar *B* (blue), moderate subsolar *B* (green), and high subsolar *B* (red). Each distribution is normalized by its number of ionograms. (f) Scatterplot of electron peak density versus the subsolar *B* for the ionospheric echoes (blue crosses) and median peak density in each bin with standard deviations (red-filled circles). In Figures 2a, 2b, 2c, and 2f, the vertical black dashed lines delimitate the groups: low ($B < 30$ nT), medium ($30 \leq B \leq 50$ nT), and high ($B > 50$ nT) subsolar *B*.

subsolar *B*. There are relatively less ionospheric echoes for $10 < B < 40$ nT compared to the data coverage, while there are relatively more ionospheric echoes for $40 < B < 80$ nT compared to the data coverage. Indeed, 14% of the ionograms from the histogram of data coverage in Figure 2a correspond to subsolar $B > 50$ nT, and 34.5% to subsolar $B < 30$ nT. The data coverage is thus 2.5 times denser for the low subsolar *B* range than for the high subsolar *B* range, but with a similar number of ionospheric echoes in both cases.

We then look in Figure 2c at the occurrence frequency of measuring ionospheric echoes with peak densities high enough to be detected, in 10° size bins of subsolar *B*. The occurrence frequency in a given bin is the number of ionospheric echoes in that bin divided by the number of ionograms in the data coverage in that bin. The ionosphere is more frequently detected in the moderate subsolar *B* range (median frequency of 13%) than in the low subsolar *B* range (8%). In the high subsolar *B* range, the frequency is even higher (19%), although there is a data bin without an ionospheric echo, due to the low statistics. Thus, it seems that the peak electron density is more often high enough to be detected during average and extreme solar wind conditions, than during quiet conditions. This suggests that the higher densities may be due to an increased strength of the ionization sources, or to a reduction in the recombination coefficient, which can happen when the ionospheric plasma temperature increases. For example, the electron impact ionization and the energy transfer from the solar wind to the atmosphere may be enhanced for the larger magnetotail and magnetosheath electron fluxes, associated with the passage of solar wind pressure pulses at Mars [e.g., *Dubinin et al.*, 2009; *Nilsson et al.*, 2011].

The histogram of electron peak densities for the ionospheric echoes is displayed in Figure 2d. The distribution has a 25th percentile of $8.4 \cdot 10^3$ cm^{-3}, a median of $1.2 \cdot 10^4$ cm^{-3} and a 75th percentile of $1.6 \cdot 10^4$ cm^{-3}. The lowest

©2014. American Geophysical Union. All Rights Reserved.

peak density is $3.4 \cdot 10^3$ cm^{-3}, and the highest is $6.1 \cdot 10^4$ cm^{-3}. In theory, peak densities as low as ~120 cm^{-3} could be detected by MARSIS; however, the radiated power of the dipole antenna falls off rapidly with frequency for frequencies below ~0.5 MHz, so it is usually not possible to detect peak densities below ~5000 cm^{-3}. The estimated probability of detecting peak densities < 5000 cm^{-3} is lower than 0.05, from Figure 6a in *Němec et al.* [2010]. In our Figure 2d, the measured peak densities are often well above the measurement threshold of MARSIS at low frequencies, about 5000 cm^{-3}; note, however, that only 11% of the ionograms display an ionospheric echo, which indicates that most of the nightside peak densities actually fall below ~5000 cm^{-3} [*Němec et al.*, 2010].

In Figure 2e, the histogram of the electron peak density is shown for three data groups: low subsolar *B* (blue), moderate subsolar *B* (green), and high subsolar *B* (red). The low subsolar *B* histogram is shifted to lower peak densities compared to the high subsolar *B* histogram. The median value is $1.1 \cdot 10^4$ cm^{-3} for the low subsolar *B* group, $1.2 \cdot 10^4$ cm^{-3} for moderate subsolar *B*, and $1.4 \cdot 10^4$ cm^{-3} for high subsolar *B*. The low subsolar *B* and the high subsolar *B* groups both have a significant second population at densities $> 10^{4.5} = 3.2 \cdot 10^4$ cm^{-3}, which will be examined in more detail later.

Figure 2f shows a scatterplot of the electron peak density versus subsolar *B*. There is a significant scatter in peak density for subsolar $B < 70$ nT, while the median values of peak density do not vary significantly with subsolar *B*, remaining close to $1 \cdot 10^4$ cm^{-3}. This is consistent with the fact that the medians of the histograms in Figure 2e are also near $1 \cdot 10^4$ cm^{-3} and that all three groups of subsolar *B* display a similar extended range of densities varying over roughly 1 order of magnitude. We interpret these results to imply that moderate and extreme solar wind conditions increase the peak densities enough to be more often detectable, and indeed, the peak densities tend to be large (easily reaching $1 \cdot 10^4$ cm^{-3}) and constitute the far end of the distribution of the peak densities. The peak density thus tends to increase when the dynamic pressure is high.

The crustal magnetic field is known to control the ionization sources for the nightside ionosphere [e.g., *Němec et al.*, 2010]. We now investigate, in Figure 3, the relationship of the ionospheric echoes to the magnetic anomalies for various solar wind conditions. The figure is divided into three columns: Figures 3a, 3d, and 3g for low subsolar *B*, Figures 3b, 3e, and 3h for moderate subsolar *B*, and Figures 3c, 3f, and 3i for high subsolar *B*. The panels are organized into three rows. Figures 3a–3f show the map of the radial component of the crustal field at ~400 km altitude measured by MGS [*Connerney et al.*, 2001]. We describe Figures 3g–3i below.

In the Figures 3a–3c, the black dots are the locations of the footprints of MEX for the ionograms of the data coverage. The data coverage is most dense for the moderate subsolar *B* group (Figure 3b), less dense for the low subsolar *B* group (Figure 3a) and least dense for the high subsolar *B* group (Figure 3c). For the period of study and the conditions imposed on the SZA and altitude of MEX, most of the data are sampled in the southern hemisphere, with measurements both in the weak and strong crustal field regions.

In Figures 3d–3f, the black crosses are the locations of the footprints of MEX for the ionospheric echoes. We note that the nightside echoes are usually oblique [*Němec et al.*, 2010]. *Němec et al.* [2011] have determined the most probable location of series of consecutive oblique echoes, by assuming that the sources of the echoes are localized, in regions where the magnetic field configuration is likely to be open, allowing electrons to precipitate and create local ionization patches. According to Figure 3 of *Němec et al.* [2011], the most probable location of the sources of oblique echoes lie within a few degrees of the spacecraft footprint. We note that at the global scale of the maps in our Figure 3, a few degrees difference in the location of the echoes would not be visible. We therefore make no attempt to determine which echoes are vertical or oblique and no attempt to constrain the most probable location of the echoes. The ionospheric echoes are found in weak field regions and also in strong field regions, and the stretches (bands) of echoes come from the pattern of MEX orbits.

Figures 3g–3i show the location of the footprint of MEX for the ionospheric echoes, colored by the electron peak density. When comparing the maps at low subsolar *B* (Figure 3g) and high subsolar *B* (Figure 3i), we see relatively more blue crosses in Figure 3g and relatively more light green crosses (especially at high latitude) in Figure 3i. This agrees with the shift of the histograms of peak densities to higher densities for the high subsolar *B* group and to lower densities for the low subsolar *B* group, seen in Figure 2e. In all three groups of subsolar *B* (Figures 3g–3i), there are clusters of very high peak density values (red crosses). The clusters have densities $\geq 10^{4.5} = 3.2 \cdot 10^4$ cm^{-3} and constitute the second population noted in Figure 2e. These clusters are located above both strong and weak crustal field regions. They are marked by their orbit numbers.

©2014. American Geophysical Union. All Rights Reserved.

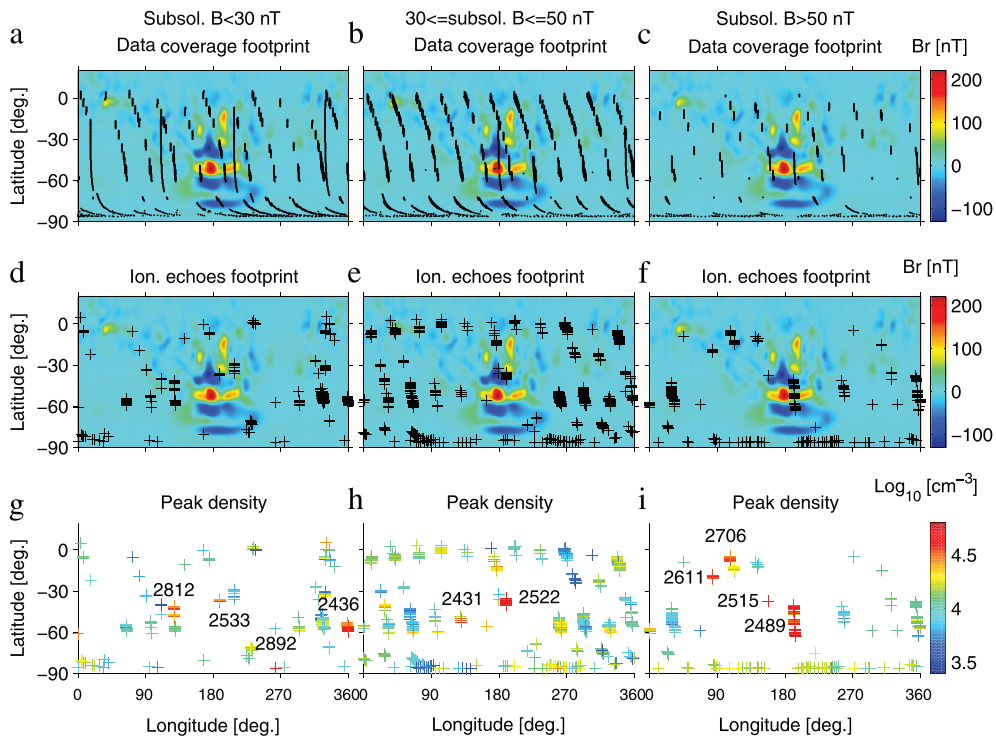

Figure 3. (a–c) Map of the radial component of the crustal magnetic field measured at ~400 km by MGS [from *Connerney et al.*, 2001], with the footprint of MEX superposed for the ionograms of the data coverage (black dots) for the low subsolar *B* group in Figure 3a, the moderate subsolar *B* group in Figure 3b, and the high subsolar *B* group in Figure 3c. (d–f) Identical to Figures 3a–3c but with the footprint of MEX superposed for the ionograms with ionospheric echoes (black crosses). (g–i) Map of the location of the footprint of MEX for the ionograms with ionospheric echoes (crosses), colored by the electron peak density. The orbit numbers are indicated for the echoes with peak density $> 10^{4.5}$ cm^{-3} (red crosses).

3.2. Dependence on IMF Clock Angle

Figure 4 investigates the dependence of ionospheric echoes on the IMF clock angle. Figure 4a shows a histogram of the clock angle values attributed to all the ionograms of the data coverage. The vertical dashed lines divide the plot into the two IMF sectors, by using the eastward or westward component of the draped IMF azimuth angle: eastward (angle $< 90°$ or angle $> 270°$) and westward ($90° <$ angle $< 270°$). The clustering of angles near 250°–270°, noted by *Brain et al.* [2006b], is evident and occurs when the upstream IMF is westward. There are 4244 ionograms in the eastward IMF group and 4291 ionograms in the westward IMF group. Figure 4b compares the distributions of clock angle values corresponding to the data coverage (black) and to the ionospheric echoes (red), with each distribution normalized by its number of ionograms. There are 483 ionospheric echoes for the eastward IMF group and 502 for the westward IMF group. There is no difference between the data coverage and the ionospheric echoes, in terms of occurrence rate.

We then look in Figure 4c at the occurrence frequency of measuring ionospheric echoes with peak densities high enough to be measured, in 15° size bins of clock angle. There is an outlier value of 46% between 105 and 120° angle, which is not statistically significant because of the low number of ionograms, compared to other bins. If we ignore this outlier, the occurrence frequency of measuring ionospheric echoes remains relatively constant over the clock angle, with a median of 10%. This confirms the lack of dependency of the occurrence rate of ionospheric echoes relative to the IMF clock angle, seen in Figure 4b.

Figure 4d is a repetition of Figure 2d, for comparison. In Figure 4e, the histograms of the electron peak density is shown for two data groups: eastward IMF (black) and westward IMF (red). The westward IMF histogram is shifted to slightly higher peak densities compared to the eastward IMF histogram. The median value is $1.1 \cdot 10^4$ cm^{-3} for the eastward IMF group and $1.3 \cdot 10^4$ cm^{-3} for westward IMF. The westward IMF distribution extends over a larger range of peak densities than the eastward IMF group: there is a significant second population

©2014. American Geophysical Union. All Rights Reserved.

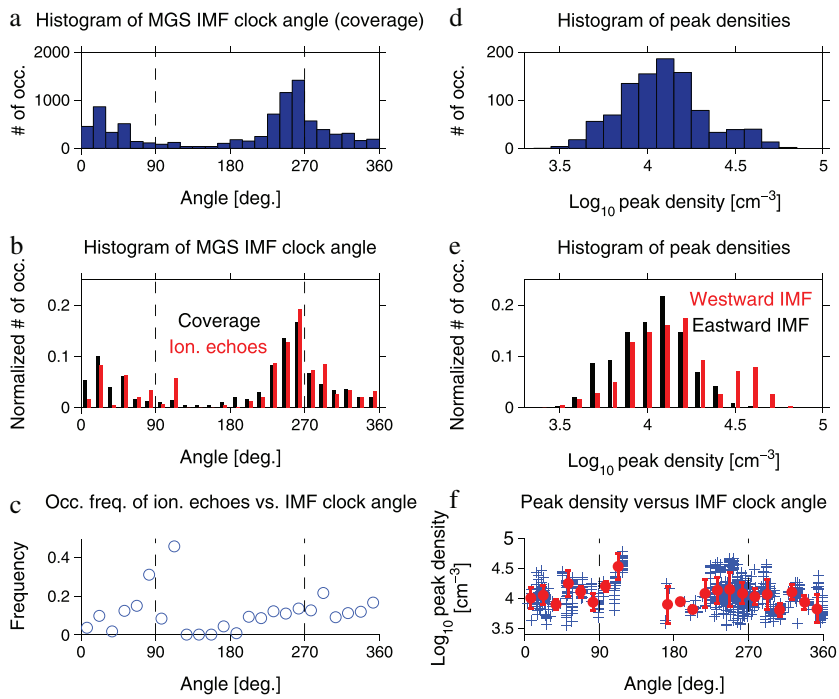

Figure 4. (a) Histogram of IMF clock angle values assigned to the ionograms of the data coverage. The bin size is 15°. (b) Histograms of IMF clock angle values assigned to the ionograms of the data coverage (black) and to the ionograms with ionospheric echoes (red). Each distribution is normalized by its number of ionograms. (c) Occurrence frequency of detecting ionospheric echoes binned by the IMF clock angle. (d) Histogram of electron peak densities for the ionospheric echoes. (e) Histograms of electron peak densities for the ionospheric echoes, sorted into two groups: eastward IMF (black) and westward IMF (red). Each distribution is normalized by its number of ionograms. (f) Scatterplot of electron peak density versus the IMF clock angle for the ionospheric echoes (blue crosses) and median peak density in each bin with standard deviations (red-filled circles). In Figures 4a, 4b, 4c, and 4f, the vertical black dashed lines delimitate the two IMF sectors, eastward (angle $<$ 90° or angle $>$ 270°) and westward (90° $<$ angle $<$ 270°).

at densities $> 10^{4.5}$ cm^{-3} for westward IMF but not for eastward IMF. Thus, the observation of very high values of peak densities is favored for a particular IMF orientation.

Figure 4f shows a scatterplot of the electron peak density versus IMF clock angle. There is a significant scatter in peak density, while the median values of peak density are relatively constant with the IMF clock angle, remaining close to $1.1 \cdot 10^4$ cm^{-3}. The population with very high densities $> 10^{4.5}$ cm^{-3} is predominant in the westward IMF group.

We also show the maps of ionospheric echoes for the two IMF groups in Figure 5. The figure has three rows in a similar format as Figure 3 but with two columns: the Figures 5a, 5c, and 5e for the eastward IMF group and Figures 5b, 5d, and 5f for westward IMF. One sees an even data coverage between the two IMF groups (Figures 5a and 5b), and also an even spread of the ionospheric echoes (Figures 5c and 5d), covering both regions of weak and strong crustal fields. The very high density echoes $> 10^{4.5}$ cm^{-3} are mostly present in the westward IMF group (Figure 5f) and almost absent from the eastward IMF group (Figure 5e). The red crosses are found both above strong and weak crustal fields. For densities $< 10^{4.5}$ cm^{-3} there is no striking difference in peak density distribution between the two groups, just relatively more echoes with low peak density (dark blue crosses) for eastward IMF than for westward IMF.

The preferred observation of the very high peak density echoes for a particular IMF orientation, suggests there may be an asymmetry in the spatial distribution of peak densities relative to the direction of the solar wind convection electric field Esw = −Vsw × Bsw, where Vsw is the solar wind bulk velocity vector and Bsw is the IMF vector in the solar wind. To check this effect, we select the MGS/MAG-ER magnetic field measurements between 2 h before and after the times of each ionogram, when MGS is on the dayside, in the latitude band 50°–60° where the magnetic field is mostly of solar wind origin. If such measurements do exist, the average-draped IMF direction is estimated by using the magnetic field vector components in the

©2014. American Geophysical Union. All Rights Reserved.

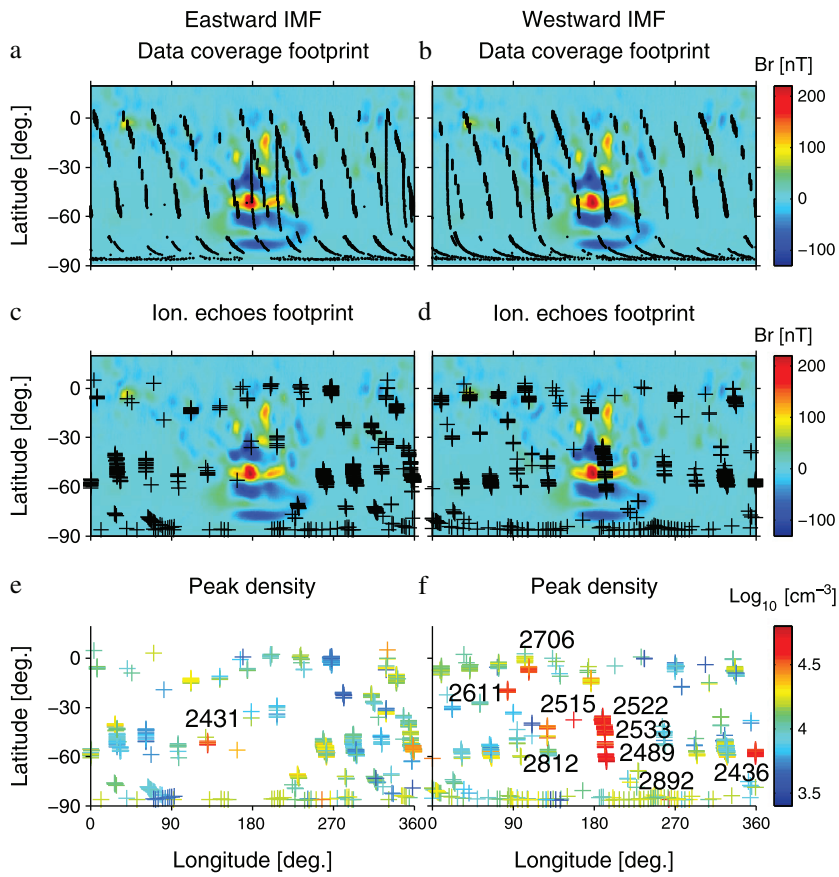

Figure 5. (a, b) Map of the radial component of the crustal magnetic field measured at ~400 km by MGS [from *Connerney et al.*, 2001], with the footprint of MEX superposed for the ionograms of the data coverage (black dots) for the eastward IMF group in Figure 5a and the westward IMF group in Figure 5b. (c, d) Identical to Figures 5a and 5b but with the footprint of MEX superposed for the ionograms with ionospheric echoes (black crosses). (e, f) Map of the location of the footprint of MEX for the ionograms with ionospheric echoes (crosses), colored by the electron peak density. The orbit numbers are indicated for the echoes with peak density $> 10^{4.5}$ cm^{-3} (red crosses).

plane perpendicular to the Mars-Sun line and assuming this is a good approximation of the upstream IMF direction. The convection electric field is calculated from the estimated IMF direction, assuming that the solar wind flow is along the Mars-Sun line (the aberration angle of the solar wind flow relative to Mars motion is neglected). Under these conditions, the directions of IMF and Esw have been assigned to 8535 ionograms of the data coverage. The location of MEX for these ionograms has been rotated into the Cartesian right-handed Mars Solar Electric field frame and shown in Figure 6. In each panel of Figure 6, Mars is viewed in this frame, from the Sun. The data are projected into the plane perpendicular to the Mars-Sun line direction. The horizontal axis and the vertical axis are the estimated IMF and Esw directions, respectively.

Figure 6a shows the data coverage around Mars. The color in each bin is the number of ionograms per bin. The coverage forms a circular shape because it covers the close nightside (SZA $< 130°$), but not the deep nightside behind the planet. The coverage is better on the right side of the panel, than on the left side (this is an effect of the clustering of draped IMF directions toward southwest). For the next panels, only the bins with at least 150 ionograms will be taken. We define the + Esw hemisphere (−Esw hemisphere) as the hemisphere where Esw points away from (toward) the surface of Mars, represented by the positive (negative) values on the vertical axis. The coverage is quite even in the two hemispheres.

The IMF and Esw directions have been assigned to 985 ionospheric echoes. The occurrence frequency of measuring ionospheric echoes with peak densities above the detection threshold is shown in Figure 6b. The panel indicates no Esw asymmetry and thus again no dependence on IMF orientation. We will examine this result in section 4.

©2014. American Geophysical Union. All Rights Reserved.

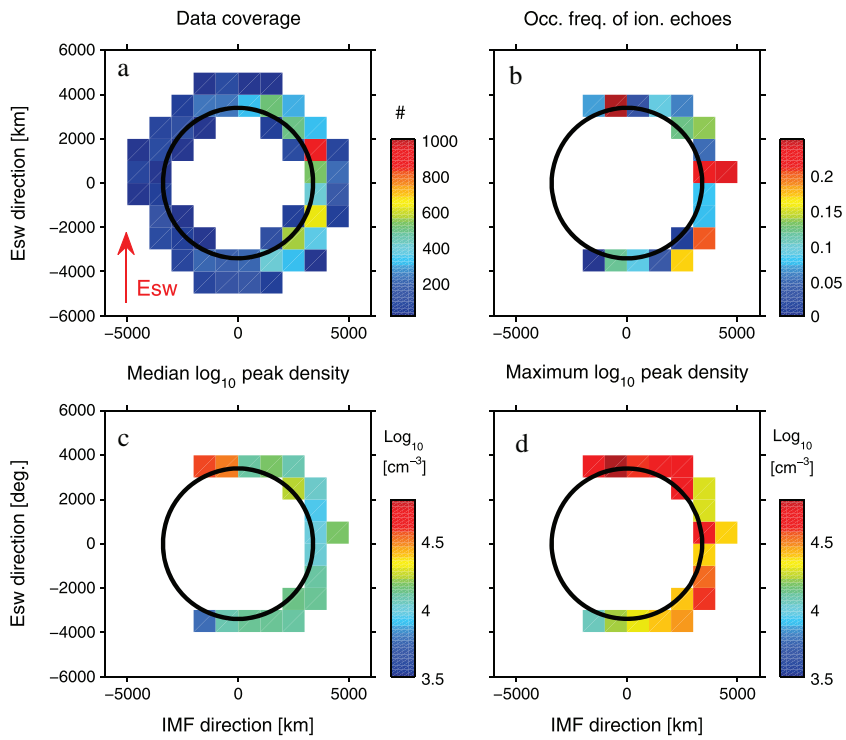

Figure 6. Each panel is a view from the Sun, with the data projected into the terminator plane normal to the Sun-Mars direction. The location of the data is binned (1000 · 1000 km bin size) in the Mars Solar Electric frame, where the horizontal axis points along the IMF vector direction estimated from MGS (see detail in the text) and the vertical axis points along the solar wind convection electric field Esw = −Vsw × Bsw. The black circle represents Mars. (a) Data coverage showing the number of ionograms in each bin. In the next panels, the bins with less than 150 ionograms are not used. (b) Occurrence frequency of detecting ionospheric echoes. (c, d) Median and maximum electron peak density per bin, respectively.

Figures 6c and 6d represent the median and the maximum values, respectively, of the electron peak density in each bin of the Esw frame. The highest peak densities are found predominantly in the + Esw hemisphere, i.e., they are predominantly observed for the westward IMF orientation in the South hemisphere (Figure 5f).

The asymmetry of the spatial distribution of peak densities relative to the convection electric field gives hints that the ionization sources responsible for these echoes are also affected by the electric field. We remark that suprathermal electron spikes are reported on nightside above the large magnetic anomalies when the IMF points dawnward (westward), [e.g., *Dubinin et al.*, 2008b]. In addition, accelerated inverted-V electrons are found near strong crustal fields, predominantly in the + Esw hemisphere [e.g., *Brain et al.*, 2006a]. The occurrence of these electron signatures is controlled by the IMF orientation. This suggests that magnetic reconnection can occur between the crustal fields and the IMF, at the boundary between closed and open field lines, allowing precipitating electrons to reach low altitudes in cusp regions and ionize the atmosphere [e.g., *Brain et al.*, 2006a]. We here make the hypothesis that the main ionization source associated with the highest peak densities is the precipitation of suprathermal electrons.

3.3. Ionospheric Echoes With Very High Peak Electron Density

We have made a list of 10 MEX orbits presenting clusters of ionospheric echoes with electron peak densities $> 10^{4.5}$ cm^{-3}, whose orbit numbers are indicated in Figures 3 and 5. The list is presented in Table 1. We have checked whether there are simultaneous measurements by the Electron Spectrometer (ELS) instrument, part of the Analyzer of Space Plasmas and Energetic Atoms (ASPERA-3) particle package onboard MEX [*Barabash et al.*, 2006]. In this work, ELS measures 2-D electron distributions in the energy range 5 eV–20 keV (energy resolution $\Delta E/E = 8\%$) at 4 s time resolution. The ELS electron spectra measured during the times of the echoes are classified by visual inspection of their energy and flux ranges and by using the position of MEX relative to the planet and to the plasma boundaries.

©2014. American Geophysical Union. All Rights Reserved.

Table 1. List of MEX Orbits With at Least One Ionospheric Echo With Electron Peak Density $> 10^{4.5}$ cm^{-3}

Orbit #	Date, Time	SZA Range (deg)	Altitude Range of MEX (km)	Crustal *B* Range 400 km (nT)	Subsolar *B* (nT)	IMF Clock Angle (deg)	Electron Peak Density Range (cm^{-3})	ELS Electron Spectrum	Median ELS Particle Flux in 40–80 eV[a] Range for All Anodes (cm^{-2} s^{-1})
2431	4 Dec. 2005, 9 h 33:06–9 h 33:36 UT	114.7–116.	1028–1068	5.–13.5	45.15	292.	3.2 10^4–3.7 10^4	Accelerated electrons 8:47:00–9:33:30 UT	$4.6 \cdot 10^8$
2436	5 Dec. 2005, 19 h 09:36–19 h 11:06 UT	108.4–112.4	818–929	10.1–14.6	22.25	246.6	3.3 10^4–4.7 10^4	No ELS data	None
2489	20 Dec. 2005, 15 h 06:35–15 h 13:52 UT	107.4–125.25	575–1085	47.6–98.85	62.45	118.1	3.2 10^4–6.1 10^4	Accelerated electrons 14:58:00–15:08:30 UT, reduced magnetotail electron fluxes 15:08:30–15:12:00 UT, ionospheric electrons after 15:12:00 UT	$1.1 \cdot 10^9$ [b]
2515	27 Dec. 2005, 21 h 46:27 UT	126.8	1044	57.4	74.45	256.2	3.7 10^4	Accelerated electrons/electron spikes 21:24:00–21:57:00 UT	$1.5 \cdot 10^9$
2522	29 Dec. 2005, 20 h 47:30–20 h 49:16 UT	124.9–128.1	936–1074	68.3–101.7	46.7	252.1	3.2 10^4–4.6 10^4	Accelerated electrons 20:35:00–20:54:00 UT	$3.8 \cdot 10^8$
2533	1 Jan. 2006, 22 h 42:43–22:42:58 UT	125.9–126.3	941–960	85.95–90.9	23.9	230.0	3.2 10^4–3.7 10^4	Accelerated electrons 22:33:00–22:47:30 UT	$2.7 \cdot 10^8$
2611	23 Jan. 2006, 18 h 44:44–18 h 45:21 UT	127.7–128.1	1049–1099	6.7–8.2	81.9	250.6	3.2 10^4–3.9 10^4	Magnetic pileup region electrons at 18:44:44–18:45:21 UT	$8.8 \cdot 10^8$
2706	19 Feb. 2006, 9 h 11:07–9 h 12:00 UT	116.3–116.55	933–1001	18.9–27.3	56.3	236.4	3.3 10^4–3.6 10^4	Accelerated electrons 9:08:30–9:15:00 UT	$1.8 \cdot 10^9$
2812	21 Mar. 2006, 1 h 51:30–1 h 53:16 UT	107.6–108.	286–291	5.55–24.7	28.6	224.1	3.2 10^4–3.6 10^4	Electron spikes/accelerated electrons 1:48:30–1:53:00 UT	$2.7 \cdot 10^8$
2892	12 Apr. 2006, 11 h 43:50 UT	108.6	1099	5.32	28.3	233.2	3.4 10^4	Magnetic pileup region electrons at 11:43 UT	$2.5 \cdot 10^8$

[a]Although electrons with energies below and above the 40–80 eV range can cause heating and ionization of the atmosphere, we choose this range for two reasons: it is typical for solar wind type electron spectra observed on nightside and because we make comparisons with results from *Dubinin et al.* [2008b] in section 4.

[b]The median electron particle flux value is for the period 15:06:34–15:08:31 UT, which is part of the period when the ionosphere echoes are detected coincident with accelerated electrons. For the other orbits, the median value is for the entire periods of the ionospheric echoes.

©2014. American Geophysical Union. All Rights Reserved.

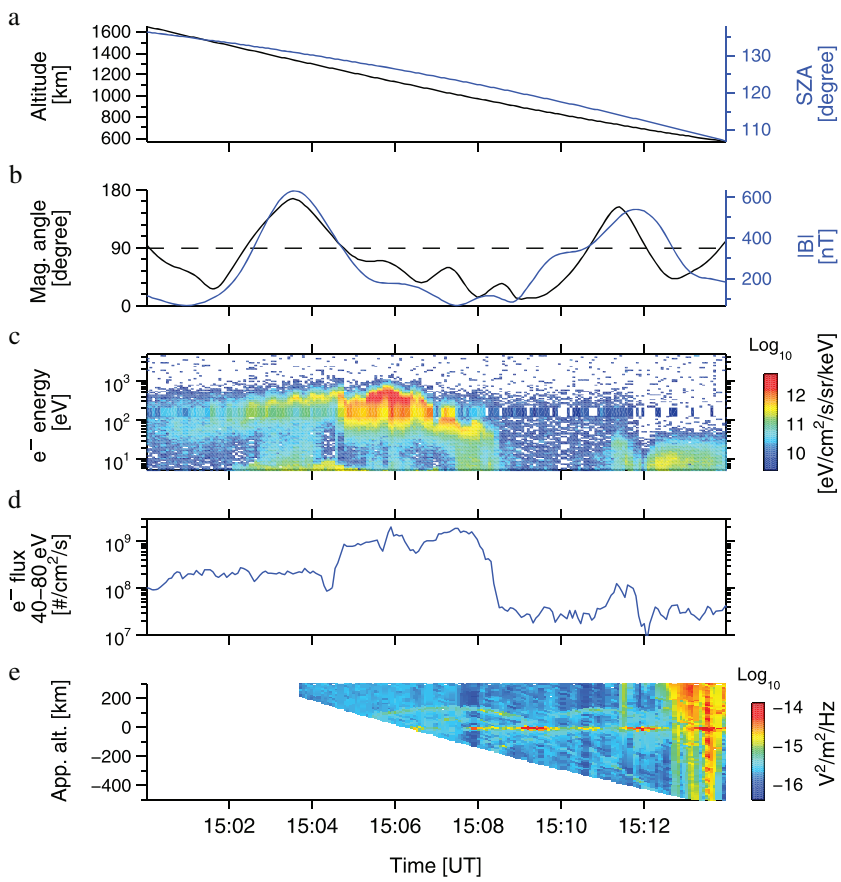

Figure 7. Time series on 20 December 2005, 1500–1514 UT, during orbit 2489. (a) Altitude (black) and SZA (blue) of MEX. (b) Magnetic field strength (blue) and angle of the magnetic field vector relative to the nadir direction (black), from the *Cain et al.* [2003] model at 150 km altitude. Zero degrees is vertical downward and 180° is vertical upward. (c) Electron energy time spectrogram from MEX/ASPERA-3/ELS. The vertical axis is the electron energy. The color is the differential energy flux averaged over anodes 4–8. (d) Electron particle flux integrated over all anodes and the energy range 40–80 eV. (e) MARSIS echogram. The vertical axis is the apparent altitude for the received signal (spacecraft altitude minus the range of the echo). The color is the received signal intensity averaged over the frequency range 0.5–2 MHz.

From Table 1, we see that the clusters of ionospheric echoes are found over an extended range of SZA, from 107° to 128°, with MEX altitudes around 900–1000 km (we note that 82% of the ionograms of the data coverage is taken at MEX altitudes > 900 km). Nine clusters have a westward IMF orientation (all except orbit 2431); while there is no preferred occurrence of the clusters for a particular subsolar *B* group. This indicates that the measurements of very high peak densities are well organized by the IMF direction but have no dependence on the dynamic pressure. Nine clusters have ELS data (all except orbit 2436). We see also that seven clusters are coincident with observations of suprathermal electron spikes and/or extended periods of accelerated/peaked electrons from a few minutes up to a half hour and are present in all three groups of subsolar *B*. Out of these seven clusters, four clusters have a spacecraft footprint in regions with crustal field strength > 50 nT (orbits 2489, 2515, 2522, and 2533) and three clusters in regions of crustal field strength < 50 nT (orbits 2431, 2706, and 2812), at 400 km altitude. The two other clusters having ELS data are found in regions of crustal field strength < 50 nT at 400 km. One (orbit 2611) has a high subsolar *B* value and the other (orbit 2892) has a low subsolar *B* value; both are coincident with magnetic pileup region electrons (heated spectra with energies from ~10 eV to ~100 eV, presenting a mixing of ionospheric and solar wind electrons). We will now have a closer look at two orbits from the list in Table 1, one orbit with magnetic pileup region electrons (2611) and one with accelerated electrons (2489), for example.

Figure 7 shows a time series during orbit 2489, from 1501 to 1514 UT. Panel a is the altitude and SZA of MEX. Panel b is the magnetic field strength and the angle of the magnetic field vector relative to nadir, from the

©2014. American Geophysical Union. All Rights Reserved.

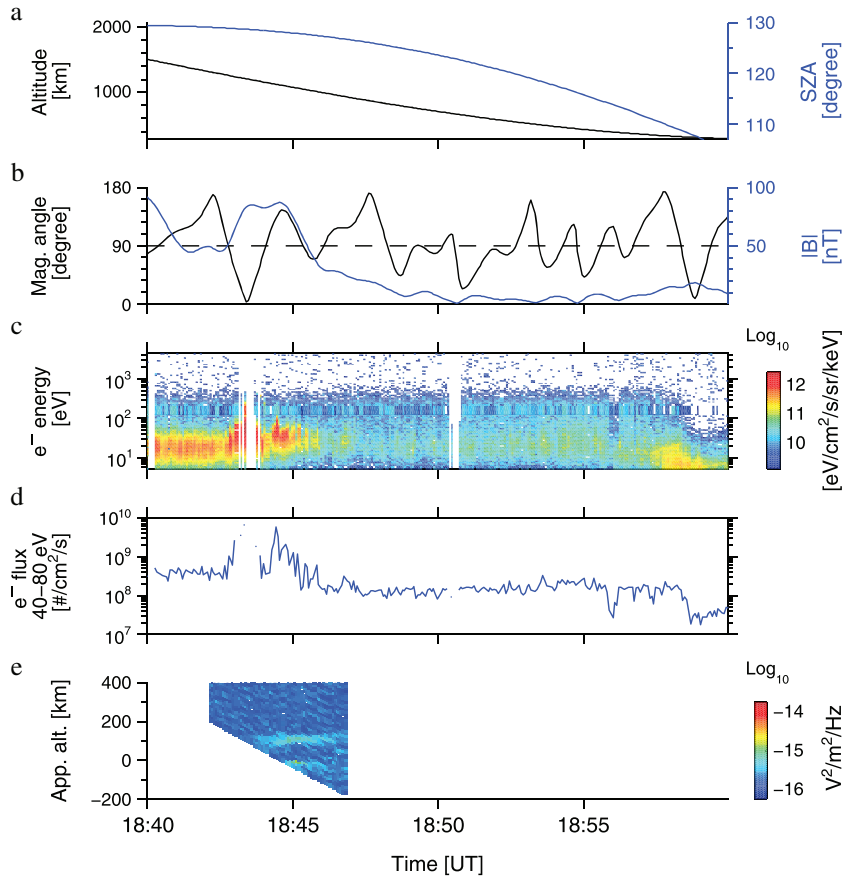

Figure 8. Time series on 23 January 2006, 1840–1900 UT, during orbit 2611. Same format as Figure 7.

Cain et al. [2003] model at 150 km altitude. Figure 7c is the electron energy time spectrogram in units of differential energy flux, averaged over sectors 4–8. Figure 7d is the electron particle flux integrated over all sectors and over 40–80 eV. Finally, Figure 7e is the echogram of received signal intensity by MARSIS, averaged over 0.5–2 MHz. During the period shown the altitude of MEX changes from 1600 to 600 km and the SZA goes from 140 to 107° (Figure 7a). The model crustal magnetic field strength at 150 km altitude varies between moderate and strong values during this pass, from 90 to 600 nT, as the spacecraft flies above the large southern magnetic anomaly, and an alternation of cusps (vertical field) and magnetic arcades (horizontal field) is seen as rapid changes in the predicted magnetic zenith angle (Figure 7b). The MARSIS data start slightly before 1504 UT, and the decrease in MEX altitude permits us to see the ground trace appearing as a horizontal line at the bottom from ~1506 UT (Figure 7e). Several hyperbola shaped traces, characteristic of oblique ionospheric echoes reflected by several point sources, are observed from 1505 UT; two main hyperbolas are seen with apex at 1507 and 1511 UT, respectively, at an apparent altitude of 150 km. After 1512 UT, we see a strong signal at almost all apparent altitudes (i.e., time delays) caused by the harmonics of the local plasma frequency. Figure 7e indicates a period of accelerated electrons from 1500 UT to slightly after 1508 UT: an inverted-V structure, identified by the inverted-V shape of the electron peak energy. This type of electron spectra was previously reported at Mars by, e.g., *Dubinin et al.* [2008b] and *Lundin et al.* [2006a, 2006b], associated with downward acceleration of electrons and upward acceleration of ions by electric fields parallel to open magnetic field lines connecting the solar wind and the crustal fields. From ~1508 to 1511 UT, we see low-magnetotail electron fluxes (perhaps reduced by the shielding of the strong crustal fields) and finally the ionospheric electrons (spectra presenting CO_2 photoelectron peaks at 21–24 and 27 eV [*Frahm et al.*, 2006] and a sharp drop off at energies above ~60 eV) from 1511 UT to the end of the plot. In Figure 7d, the electron particle flux in the energy range 40–80 eV reaches 10^8 cm^{-2} s^{-1} until 1505 UT, then increases up to 10^9 cm^{-2} s^{-1} until the end of the inverted-V structure, and finally drops after 1508 UT to 10^7 cm^{-2} s^{-1}

©2014. American Geophysical Union. All Rights Reserved.

during the periods of magnetotail fluxes and ionospheric fluxes. There are several occurrences of model vertical crustal field (1502, 1504, and 1507–1508 UT) at 150 km altitude during the period of accelerated electrons, implying that the downgoing part of the electron distribution may travel along the open field lines of the cusps down to the atmosphere and is expected to create substantial ionization there and thus high peak densities.

Figure 8 shows a time series during orbit 2611, from 1840 to 1900 UT, in the same format as Figure 7. During this period, the altitude of the spacecraft decreases from 1500 to 300 km, while the SZA changes from 130 to 107° (Figure 8a). The model crustal field strength at 150 km altitude decreases almost monotonically from 100 nT to a few nT and the calculated magnetic zenith angle changes quickly, so the overall magnetic field is moderate to low (Figure 8b) and implies that the IMF dominates the magnetic field topology. In Figure 8e, the echogram lasts from 1842 to 1847 UT; the ground trace and an ionospheric trace are visible as horizontal lines at the bottom and at 150 km, respectively, during almost the whole duration of the echogram. In Figure 8c, MEX is first located in the magnetic pileup region and meets a period of enhanced flux (burst) between 1843 and 1846 UT. From 1846 UT MEX flies into the magnetotail and approaches the planet toward the terminator until 1858 UT. At this point, MEX enters the ionosphere. In Figure 8d, the electron particle flux between 40 and 80 eV in the magnetic pileup region reaches $10^8\,\mathrm{cm}^{-2}\,\mathrm{s}^{-1}$ until 1843 UT, after which there is the electron burst where the flux goes up to $10^9\,\mathrm{cm}^{-2}\,\mathrm{s}^{-1}$ then from 1846 UT the flux decreases to $10^8\,\mathrm{cm}^{-2}\,\mathrm{s}^{-1}$ in the magnetotail. Finally, the flux drops to $10^7\,\mathrm{cm}^{-2}\,\mathrm{s}^{-1}$ after 1858 UT when MEX enters the ionosphere. The ionospheric echoes are seen simultaneously with the electron burst, at a time of moderate (80 nT) vertical crustal field. The flux measured during the electron burst may be sufficient to create the plasma patch of very high peak density if open field lines connecting the magnetic cusp and the IMF allow the downgoing part of the electron distribution to travel down to 140–160 km: the altitude range of the main nightside ionospheric layer, according to the model of, e.g., *Fillingim et al*. [2007].

4. Discussion and Conclusion

We have performed a statistical study of the Martian nightside ionosphere, using remote ionospheric sounding by MEX/MARSIS and the IMF clock angle and dynamic pressure proxies by MGS/MAG-ER, for the period November 2005 to May 2006. The results are listed as follows.

The ionospheric echoes are found both in regions of strong and low crustal magnetic fields (Figures 3 and 5), with the data coverage being mostly in the southern hemisphere, without preference for a particular location (certainly because of the scarce spatial coverage). The occurrence rate of detecting ionospheric echoes with peak densities high enough to be measured is 19% and 8%, during high and low dynamic pressure conditions, respectively (Figure 2). The occurrence rate does not depend on the IMF clock angle (Figures 4 and 6).

The peak densities which are detected are rather high, with a median of $1.2 \cdot 10^4\,\mathrm{cm}^{-3}$, which can be explained by the measurement limitations of MARSIS at low sounding frequencies. Clusters of echoes with very high peak densities ($\mathrm{Ne}_{\mathrm{max}} > 10^{4.5} = 3.2 \cdot 10^4\,\mathrm{cm}^{-3}$) are noticed in all groups of dynamic pressure, located in weak and strong crustal field regions, and corresponding to westward IMF conditions for 9 out of 10 clusters (Figures 2–5). That these very high density clusters are measured in the southern hemisphere means that almost all are found in the + Esw hemisphere (Figure 6). The Esw asymmetry implies a constraint on the origin of the ionization. Nine clusters have simultaneous in situ particle measurements by MEX/ASPERA-3, which show that seven clusters are measured during times of accelerated electrons or suprathermal electron spikes (Table 1 and Figure 7). We note that accelerated electrons and electron spikes are detected predominantly in the + Esw hemisphere [e.g., *Brain et al*., 2006a; *Dubinin et al*., 2008b].

We keep in mind that the location of the plasma patch sources of the clusters may be away from the spacecraft footprint. These plasma patches may be produced by electrons measured at MEX and/or electrons away from the MEX position, but in any case electrons magnetically connected through open field lines to cusp regions where they will produce ionization [e.g., *Lillis et al*., 2009]. For example, the ionospheric echoes observed after 15:08:30 UT in the cluster of orbit 2489 (Figure 7) are coincident with magnetotail electrons and later ionospheric electrons, but the accelerated electrons would be a more likely source of these high peak density echoes, as we discuss below. In this case, the spacecraft may be sampling a more extended region of accelerated spectra, located at the edge of open and closed field lines in a region of strong crustal field [e.g., *Brain et al*., 2006a]. We note that modeling of the electron precipitation cases, including the knowledge of electron pitch angle distributions and magnetic field configuration (we recall that MEX carries no magnetometer)

©2014. American Geophysical Union. All Rights Reserved.

would be needed to confirm these hypotheses. From a more general view, we note that patterns of precipitating electrons are indeed observed in longitudinal bands where the vertical crustal field is large [e.g., *Dubinin et al*., 2008b]. In addition, local upwellings of the dayside ionosphere located in regions of vertical crustal fields are reported to have a longitudinal East-West elongation [*Gurnett et al*., 2005; *Duru et al*., 2006; *Andrews et al*., 2014]. Such ionospheric structures are observed in regions of high percentage of open field lines, suggesting a link with the access of suprathermal electrons to low altitudes (D. Andrews, personal communication, 2014).

It seems that there are seven clusters of very high peak densities that may be caused by precipitating accelerated electrons, and two other clusters caused by precipitating magnetic pileup region electrons. The prevalence of peaked spectra is consistent with the modeled electron peak densities being larger for an input of accelerated electrons, compared to heated electrons such as magnetotail/magnetic pile up region electrons [e.g., *Fillingim et al*., 2007]. The median electron fluxes of 40–80 eV energy at the times of the clusters of ionospheric echoes listed in Table 1, are in the range 10^8–10^9 cm^{-2} s^{-1} and may be sufficient to create the patches of very high peak electron density. Indeed, *Dubinin et al*. [2008b] report that median values of 40–80 eV electron fluxes are 10^7–10^8 cm^{-2} s^{-1} at altitude $<$ 400 km on the nightside, while occasional fluxes $>$ 10^9 cm^{-2} s^{-1} would be sufficient to explain observed aurora emissions and easily create ionization. Finally, we note that *Leblanc et al*. [2008] report observations of aurora by the Spectroscopy for Investigation of Characteristics of the Atmosphere of Mars simultaneously with precipitating electrons seen by ASPERA-3, during orbit 2515, at 2147 and 2151 UT, close in time to the ionospheric echo (21:46:50 UT) listed in Table 1.

We will now discuss the importance of the two main plasma sources considered by modelers, in regard to our results: plasma transport from the dayside and electron precipitation [e.g., *Fox et al*., 1993]. Using radio occultation measurements, *Withers et al*. [2012] show that for SZA $<$ 115° the ionospheric peak densities and peak altitudes are consistent with dayside-nightside transport, while for SZA $>$ 115° the peak altitudes agree with modeled peak altitudes caused by electron precipitation. The data coverage of our study is limited to the near terminator region, with a median SZA of 116°. *Němec et al*. [2010] find that for SZA up to 125° the nightside peak densities decrease in regions of low crustal field when the SZA increases, suggesting the importance of plasma transport (while electron precipitation still plays a role). In this case the dominant magnetic field is the external draped field; the magnetotail electrons and the ionospheric plasma are able to move tailward along the IMF open field lines permeating the atmosphere. We note that the first measurements of the transterminator ion flow at Mars were realized by MEX [*Fränz et al*., 2010], as well as first estimates of the escape rates of CO_2 and O ionospheric photoelectrons into the magnetotail [*Frahm et al*., 2010]. In contrast, *Němec et al*. [2010] report that in regions of strong crustal field the peak densities do not depend on SZA suggesting no plasma transport but rather electron precipitation. Indeed, the vertical magnetic field seems to hinder the transterminator plasma transport but solar wind electron precipitation may be permitted in case of magnetic reconnection with the IMF, explaining the formation of a patchy ionosphere where the magnetic field is vertical [e.g., *Fillingim et al*., 2007; *Němec et al*., 2010, 2011].

Concerning the effect of the dynamic pressure, we find that the peak densities increase with the dynamic pressure, as deduced from the higher occurrence frequency of ionospheric echoes with peak densities high enough to be detected. We conducted the analysis in 2005–2006 during the approach to solar minimum. Near solar minimum the thermal pressure of the Martian ionosphere is usually too low to stand off the solar wind dynamic pressure [e.g., *Hanson and Mantas*, 1988], due to the decline in intensity of extreme ultraviolet radiation. The ionosphere thus becomes compressed to lower altitudes, which has the effect of reducing the transterminator flow of O^+ ions to the nightside, as in the case with the unmagnetized Venus at solar minimum [e.g., *Knudsen et al*., 1987]. In addition, when the dynamic pressure is high, the transport of O^+ ions to the nightside is likely to decline even more. There is an analogy with the Venus situation in which low nightside peak densities measured by Pioneer Venus Orbiter radio occultation during overpressure conditions at solar maximum suggest a decrease of the transterminator flow [e.g., *Zhang et al*., 1990]. In contrast the electron precipitation should increase when the dynamic pressure is high since the solar wind electron fluxes are more intense and penetrate deeper [e.g., *Lillis and Brain*, 2013]. The extra ionization caused by the enhanced precipitation may account for the increase of the occurrence frequency of detecting ionospheric echoes when the dynamic pressure rises, since the peak densities become high enough to be measured. This is consistent with the hypothesis of an electron impact source to explain cases of high integrated column densities between 200 and 500 km altitudes on Venus for high dynamic pressure

©2014. American Geophysical Union. All Rights Reserved.

conditions [*Zhang et al*., 1990]. Thus, electron impact ionization may become the dominant plasma source of the Martian nightside during solar minimum, at least for moderate and high dynamic pressure conditions, similarly to Venus.

Concerning the effect of the IMF orientation, we show that the clusters of peak density $> 10^{4.5}$ cm^{-3} are often associated with a given IMF sector, which indicates magnetic reconnection between the IMF and a vertical crustal field and hence an electron precipitation source for these echoes. We also report that the occurrence frequency of detecting peak densities above the MARSIS threshold of 5000 cm^{-3} does not depend on IMF orientation. It is not known whether there is a dependence of the dayside-nightside plasma transport on the IMF sector. Such dependence may have no importance if the electron precipitation source becomes more important for the nightside ionosphere. Meanwhile, previous measurements have shown that the access of solar wind electrons to low altitudes in regions of low crustal fields does not depend on the IMF sector [e.g., *Dubinin et al*., 2008b; *Lillis and Brain*, 2013], because the IMF open field lines permeate the topside ionosphere, independent of IMF clock angle.

Our two main results are the increase in electron peak density for larger dynamic pressure, and the prevalence of westward IMF sector for the detection of very high peak density cases, which seem to be often observed simultaneously with accelerated electrons. The data were obtained on the near nightside (SZA $< 130°$), and we expect the plasma transport to be important there. Nevertheless, electron impact ionization may prevail when the dynamic pressure is high enough to compress the ionosphere and also in regions of vertical crustal fields where the IMF orientation matters.

Acknowledgments
C.D., D.A.G., and D.D.M. are supported by contract 1224107 by the Jet Propulsion Laboratory. F.N. is supported by the KONTAKT II grant LH13031. The authors thank D.A. Brain for putting the Mars Global Surveyor proxy data for solar wind dynamic pressure and IMF clock angle on his website www.srpg.ssl.berkeley.edu/~brain/welcome2.html. The ASPERA-3 data and the MARSIS data are available on the Planetary Data System website.

Michael Liemohn thanks Matthew Fillingim and a reviewer for their assistance in evaluating this paper.

References

Acuña, M. H., et al. (1999), Global distribution of crustal magnetization discovered by the Mars Global Surveyor MAG/ER experiment, *Science*, *284*(5415), 790–793, doi:10.1126/science.284.5415.790.

Andrews, D. J., et al. (2014), Oblique reflections in the Mars Express MARSIS data set: Stable density structures in the Martian ionosphere, *J. Geophys. Res. Lett.*, doi:10.1002/2013JA019697, in press.

Barabash, S., et al. (2006), The Analyzer of Space Plasmas and Energetic Atoms (ASPERA-3) for the Mars Express Mission, *Space Sci. Rev.*, *126*(1–4), 113–164, doi:10.1007/s11214-006-9124-8.

Brain, D. A., F. Bagenal, M. H. Acuña, and J. E. P. Connerney (2003), Martian magnetic morphology: Contributions from the solar wind and crust, *J. Geophys. Res.*, *108*(A12), 1424, doi:10.1029/2002JA009482.

Brain, D. A., J. S. Halekas, R. Lillis, D. L. Mitchell, R. P. Lin, and D. H. Crider (2005), Variability of the altitude of the Martian sheath, *Geophys. Res. Lett.*, *32*, L18203, doi:10.1029/2005GL023126.

Brain, D. A., J. S. Halekas, L. M. Peticolas, R. P. Lin, J. G. Luhmann, D. L. Mitchell, G. T. Delory, S. W. Bougher, M. H. Acuña, and H. Rème (2006a), On the origin of aurorae on Mars, *Geophys. Res. Lett.*, *33*, L01201, doi:10.1029/2005GL024782.

Brain, D. A., D. L. Mitchell, and J. S. Halekas (2006b), Magnetic field draping direction at Mars from April 1999 through August 2004, *Icarus*, *182*, 464–473, doi:10.1016/j.icarus.2005.09.023.

Cain, J. C., B. B. Ferguson, and D. Mozzoni (2003), An n = 90 internal potential function of the Martian crustal magnetic field, *J. Geophys. Res.*, *108*(E2), 5008, doi:10.1029/2000JE001487.

Connerney, J. E. P., M. H. Acufia, P. J. Wasilewski, G. Kletetschka, N. F. Ness, H. Rème, R. P. Lin, and D. L. Mitchell (2001), The global magnetic field of Mars and implications for crustal evolution, *Geophys. Res. Lett.*, *28*(21), 4015–4018, doi:10.1029/2001GL013619.

Crider, D. H., et al. (2002), Observations of the latitude dependence of the location of the Martian magnetic pileup boundary, *Geophys. Res. Lett.*, *29*(8), 1170, doi:10.1029/2001GL013860.

Crider, D. H., D. Vignes, A. M. Krymskii, T. K. Breus, N. F. Ness, D. L. Mitchell, J. A. Slavin, and M. H. Acuña (2003), A proxy for determining solar wind dynamic pressure at Mars using Mars Global surveyor data, *J. Geophys. Res.*, *108*(A12), 1461, doi:10.1029/2003JA009875.

Dubinin, E., M. Fraenz, J. Woch, D. Winningham, R. Frahm, R. Lundin, and S. Barabas (2008a), Suprathermal electron fluxes on the nightside of Mars: ASPERA-3 observations, *Plan. Space Sci.*, *56*, 846–851, doi:10.1016/j.pss.2007.12.010.

Dubinin, E. M., M. Fraenz, J. Woch, E. Roussos, J. D. Winningham, R. A. Frahm, A. Coates, F. Leblanc, R. Lundin, and S. Barabash (2008b), Access of solar wind electrons into the Martian magnetosphere, *Ann. Geophys.*, *26*, 3511–3524, doi:10.5194/angeo-26-3511-2008.

Dubinin, E., et al. (2009), Ionospheric storms on Mars: Impact of the corotating interaction region, *Geophys. Res. Lett.*, *36*, L01105, doi:10.1029/2008GL036559.

Duru, F., D. A. Gurnett, T. F. Averkamp, D. L. Kirchner, R. L. Huff, A. M. Persoon, J. J. Plaut, and G. Picardi (2006), Magnetically controlled structures in the ionosphere of Mars, *J. Geophys. Res.*, *111*, A12204, doi:10.1029/2006JA011975.

Fillingim, M. O., L. M. Peticolas, R. J. Lillis, D. A. Brain, J. S. Halekas, D. L. Mitchell, R. P. Lin, D. Lummerzheim, S. W. Bougher, and D. L. Kirchner (2007), Model calculations of electron precipitation induced ionization patches on the nightside of Mars, *Geophys. Res. Lett.*, *34*, L12101, doi:10.1029/2007GL029986.

Fox, J. L., J. F. Brannon, and H. S. Porter (1993), Upper limits to the nightside ionosphere of Mars, *Geophys. Res. Lett.*, *20*, 1339–1342, doi:10.1029/93GL01349.

Frahm, R. A., et al. (2006), Locations of atmospheric photoelectron energy peaks within the Mars environment, *Space Sci. Rev.*, *126*, 389–402, doi:10.1007/s11214-006-9119-5.

Frahm, R. A., et al. (2010), Estimation of the escape of photoelectrons from Mars in 2004 liberated by the ionization of carbon dioxide and atomic oxygen, *Icarus*, *206*(1), 50–63, doi:10.1016/j.icarus.2009.03.024.

Fränz, M., et al. (2006), Plasma intrusion above Mars crustal fields—Mars Express ASPERA-3 observations, *Icarus*, *182*(2), 406–412, doi:10.1016/j.icarus2005.11.016.

©2014. American Geophysical Union. All Rights Reserved.

Fränz, M., E. Dubinin, E. Nielsen, J. Woch, S. Barabash, R. Lundin, and A. Fedorov (2010), Transterminator ion flow in the Martian ionosphere, *Plan. Space Sci.*, *58*(11), 1442–1454, doi:10.1016/j.pss.2010.06.009.

Gurnett, D. A., et al. (2005), Radar soundings of the ionosphere of Mars, *Science*, *310*(5756), 1929–1933, doi:10.1126/science.1121868.

Gurnett, D. A., et al. (2008), An overview of radar soundings of the Martian ionosphere from the Mars express spacecraft, *Adv. Space Res.*, *41*, 1335–1346, doi:10.1016/j.asr.2007.01.062.

Knudsen, W. C., A. J. Kliore, and R. C. Whitten (1987), Solar cycle changes in the ionization sources of the nightside Venus ionosphere, *J. Geophys. Res.*, *92*(A12), 13,391–13,398, doi:10.1029/JA092iA12p13391.

Leblanc, F., et al. (2008), Observations of aurorae by SPICAM ultraviolet spectrograph on board Mars Express: Simultaneous ASPERA-3 and MARSIS measurements, *J. Geophys. Res.*, *113*, A08311, doi:10.1029/2008JA013033.

Lillis, R. J., M. O. Fillingim, L. M. Peticolas, D. A. Brain, R. P. Lin, and S. W. Bougher (2009), Nightside ionosphere of Mars: Modeling the effects of crustal magnetic fields and electron pitch angle distributions on electron impact ionization, *J. Geophys. Res.*, *114*, E11009, doi:10.1029/2009JE003379.

Lillis, R. J., and D. A. Brain (2013), Nightside electron precipitation at Mars: Geographic variability and dependence on solar wind conditions, *J. Geophys. Res. Space Phys.*, *118*, 3546–3556, doi:10.1002/jgra.50171.

Lundin, R., et al. (2006a), Plasma acceleration above Martian magnetic anomalies, *Science*, *311*(5763), 980–983, doi:10.1126/science.1122071.

Lundin, R., et al. (2006b), Ionospheric plasma acceleration at Mars: ASPERA-3 results, *Icarus*, *182*(2), 308–319, doi:10.1016/j.icarus.2005.10.035.

Hanson, W. B., and G. P. Mantas (1988), Viking electron temperature measurements: Evidence for a magnetic field in the Martian ionosphere, *J. Geophys. Res.*, *93*, 7538–7544, doi:10.1029/JA093iA07p07538.

Morgan, D. D., D. A. Gurnett, D. L. Kirchner, J. L. Fox, E. Nielsen, and J. J. Plaut (2008), Variation of the Martian ionospheric electron density from Mars Express radar soundings, *J. Geophys. Res.*, *113*, A09303, doi:10.1029/2008JA013313.

Mitchell, D. L., R. P. Lin, C. Mazelle, H. Rème, P. A. Cloutier, J. E. P. Connerney, M. H. Acuña, and N. F. Ness (2001), Probing Mars' crustal magnetic field and ionosphere with the MGS Electron Reflectometer, *J. Geophys. Res.*, *106*(E10), 23,419–23,428, doi:10.1029/2000JE001435.

Nagy, A. F., et al. (2004), The plasma environment of Mars, *Space Sci. Rev.*, *111*, 33–114, doi:10.1023/B:SPAC.0000032718.47512.92.

Němec, F., D. D. Morgan, D. A. Gurnett, and F. Duru (2010), Nightside ionosphere of Mars: Radar soundings by the Mars Express spacecraft, *J. Geophys. Res.*, *115*, E12009, doi:10.1029/2010JE003663.

Němec, F., D. D. Morgan, D. A. Gurnett, and D. A. Brain (2011), Areas of enhanced ionization in the deep nightside ionosphere of Mars, *J. Geophys. Res.*, *116*, E06006, doi:10.1029/2011JE003804.

Nilsson, H., et al. (2011), Heavy ion escape from Mars, influence from solar wind conditions and crustal magnetic fields, *Icarus*, *215*(2), 475–484, doi:10.1016/j.icarus.2011.08.003.

Picardi, G., et al. (2004), MARSIS: Mars Advanced Radar for Subsurface and Ionospheric Sounding, in *Mars Express: A European Mission to the Red Planet*, edited by A. Wilson, pp. 51–69, ESA Publ. Div, Noordwijk, Netherlands.

Safaeinili, A., W. Kofman, J. Mouginot, Y. Gim, A. Herique, A. B. Ivanov, J. J. Plaut, and G. Picardi (2007), Estimation of the total electron content of the Martian ionosphere using radar sounder surface echoes, *Geophys. Res. Lett.*, *34*, L23204, doi:10.1029/2007GL032154.

Withers, P., M. O. Fillingim, R. J. Lillis, B. Häusler, D. P. Hinson, G. L. Tyler, M. Pätzold, K. Peter, S. Tellmann, and O. Witasse (2012), Observations of the nightside ionosphere of Mars by the Mars Express Radio Science Experiment (MaRS), *J. Geophys. Res.*, *117*, A12307, doi:10.1029/2012JA018185.

Zhang, M. H. G., J. G. Luhmann, and A. J. Kliore (1990), An observational study of the nightside ionospheres of Mars and Venus with radio occultation methods, *J. Geophys. Res.*, *95*(A10), 17,095–17,102, doi:10.1029/JA095iA10p17095.

©2014. American Geophysical Union. All Rights Reserved.